Multimode interference in circular step-index fibers studied with the mode expansion approach

Hongbo Li,[1,3,*] Moysey Brio,[2,3] Li Li,[1] Axel Schülzgen,[1] Nasser Peyghambarian,[1] and Jerome V. Moloney[1,2,3]

[1]*College of Optical Sciences, The University of Arizona, Tucson, Arizona 85721, USA*
[2]*Department of Mathematics, The University of Arizona, Tucson, Arizona 85721, USA*
[3]*Arizona Center for Mathematical Sciences, The University of Arizona, Tucson, Arizona 85721, USA*
[*]*Corresponding author: hongbo@email.arizona.edu*

Received May 14, 2007; revised August 8, 2007; accepted August 9, 2007;
posted August 9, 2007 (Doc. ID 83026); published September 24, 2007

The mode expansion approach in vectorial form, using a complete set of guided modes of a circular step-index fiber (SIF), is developed and applied to analyze multimode interference in multimode fibers (MMFs) for the first time, to the best of our knowledge. The complete set of guided modes of an SIF is defined based on its modal properties, and a suitable modal orthogonality relation is identified to evaluate the coefficients in a mode expansion. An algorithm, adaptive to incident fields, is then developed to systematically and efficiently perform mode expansion in highly MMFs. The mode expansion approach is successfully applied to investigate the mode-selection properties of coreless fiber segments incorporated in multicore fiber lasers and the self-imaging in MMFs. © 2007 Optical Society of America

OCIS codes: 060.2270, 060.2340, 140.3510, 140.3290.

1. INTRODUCTION

In a multimode step-index fiber (SIF), multiple modes can be guided along the fiber. A general incident optical field typically excites higher-order modes in addition to the fundamental modes of the fiber; consequently, the excited propagating field is a combination of guided modes and is subject to multimode interference (MMI). Due to the MMI effect, multimode fibers (MMFs) can be designed to control field propagation and therefore be utilized as MMI components in fiber optic devices. It has been demonstrated, both numerically and experimentally, that by applying the MMI theory, MMFs can be successfully designed and employed in optical devices such as fiber-optic displacement sensors [1], wavelength tunable fiber lenses [2] and lasers [3], refractometer sensors [4], bandpass filters [5], phase-locked multicore fiber lasers [6,7], etc. For photonic devices based on optical fibers, an all-fiber design is always highly desirable, considering its advantage of being compact and free of alignment. MMF-based elements fit naturally in all-fiber designs and have been proved capable of controlling the propagation of light [1–7]. To effectively design MMFs for MMI-based applications, it is crucial to be able to simulate and understand the MMI effects of MMFs.

MMI was first proposed and investigated for slab waveguides. Self-imaging in step-index slab waveguides, a phenomenon due to MMI, was proposed in [8] and later described in detail in [9]. Since then, optical devices based on MMI and self-imaging in slab waveguides have been widely used in various photonic integrated circuits for optical communications, including optical couplers, combiners, switches, modulators, filters, etc. Soldano and Pennings [10] suggested modal propagation analysis, ray optics, hybrid methods, and the beam propagation method (BPM) as potential approaches for analyzing MMI in slab waveguides. The guided-mode propagation analysis was employed by Soldano and Pennings [10] to investigate the self-imaging principle in multimode slab waveguides, which led to a number of fundamental findings. The great success in the analysis of MMI in slab waveguides can be attributed to the fact that there exists an analytical formula for evaluating the propagation constants of the guided modes of highly multimode slab waveguides [10]. In contrast, for highly multimode SIFs, the majority of the guided modes are hybrid and not linearly polarized, with no generic analytical formula available for evaluating the propagation constants. This complicates the analysis of MMI in multimode SIFs and renders the necessity of relying on numerical approaches.

Two numerical approaches have been reported in the literature regarding analyzing MMI effects and self-imaging properties of MMFs, namely, the mode expansion approach [1,2,5] and the BPM [4,11]. In [1,2,5], the fundamental scalar mode of a single-mode SIF is coupled to the center of an MMF segment, where the MMI in the MMF segment is analyzed with the mode expansion approach. In this approach, the weakly guiding approximation is adopted for the MMF, so the guided modes of the MMF, which form the basis for the mode expansion approach, are linearly polarized (LP) (or scalar). Since the amplitude of the incident scalar field is circularly symmetric with respect to the MMF, the modes excited in the MMF are circularly symmetric as well. As a result, the number of guided modes used in the mode expansion is greatly reduced. In summary, the mode expansion approach is efficient and has the inherent advantage of avoiding numerical error accumulation when the length of the MMF increases. Given that only circularly symmetric modes are used, this approach, however, cannot be applied to study, e.g., the effect of misalignments between

the single-mode fiber (SMF) segment and the MMF segment [5]. In [4,11], MMI in the MMF segment of an SMF-MMF-SMF structure is investigated with the BPM, where the optical field inside the structure is assumed to be linearly polarized and the scalar wave equation is solved accordingly. Considering the circular symmetry of the structure, the optical field is further simplified to be independent of the angular coordinate in the cylindrical coordinate system. The Padé approximation is employed in the finite-difference scheme to ensure the accuracy of the BPM if the propagating field contains large angle components. Since the BPM makes use of the circular symmetry of the fiber structure and assumes that the optical field is linearly polarized with circularly symmetric amplitude, this approach, like the mode expansion approach in [1,2,5], is not applicable to cases where misalignments between different fiber segments need to be considered.

The vectorial finite-difference beam propagation method (VFDBPM) is a more general approach and capable of analyzing the effect of misalignments between different fiber segments. However, VFDBPM relies on finite-difference schemes for discretization of the transverse domain of a given structure, and therefore treats discontinuity in the material and nongrid aligned boundaries separately. The vectorial finite-element beam propagation method (FE-BPM), being an integral formation on an irregular grid of the transverse domain of a structure, can be used as an alternative to VFDBPM to overcome the above-mentioned disadvantages of finite-difference BPMs. In both methods, the matrix exponent of beam propagation is represented with Taylor or Padé approximation, leading to linear increases in numerical errors as the propagation distance increases. This is illustrated in Section 4, where the vectorial FE-BPM is employed to analyze MMI in MMFs. Therefore, no matter how accurately a numerical discretization can be devised for the VFDBPM or vectorial FE-BPM, the fundamental disadvantage of error accumulation with propagation distance is unavoidable.

In this paper, the mode expansion approach in vectorial form, using a complete set of guided modes of a multimode SIF, is developed and employed to analyze MMI in MMFs for the first time, to the best of our knowledge. Unlike the scalar approaches presented in the literature, the vectorial mode expansion approach can be applied to analyze the MMI of an optical field that is noncircularly symmetric to its host MMF. To systematically calculate the guided modes of an SIF with computer procedures, the modal characteristics of the SIFs are explored in detail, and a set of simplified formulas is derived for describing the electromagnetic field of the guided mode with a given propagation constant. The guided modes with negative angular orders, being largely neglected in the literature, are elaborated to form the complete set of the guided modes of an SIF for the mode expansion approach. To evaluate the coefficients in a mode expansion, a suitable orthogonality relation for the guided modes used in this study is identified and verified both analytically and numerically. Since a large number of guided modes are allowed in an MMF for MMI applications, an adaptive algorithm is developed in Section 3 to perform mode expansion of optical fields in highly MMFs systematically and efficiently. In Section 4, the mode expansion approach developed in this study is validated by utilizing it to analyze MMI in two MMF-based components, namely, the coreless fiber segment for mode selection in a multicore fiber (MCF) laser [6,7] and the MMF segment in an SMF-MMF-SMF structure [4,5]. The results in Section 4 show that the vectorial mode expansion approach can capture the polarization effect on MMI that cannot be resolved by scalar approaches.

2. MODAL PROPERTIES AND ORTHOGONALITY RELATION

For circular SIFs the optical field and the corresponding propagation constant of a guided mode can be solved rigorously. The analytical formulas describing the field and the characteristic equations for the propagation constant have been presented in the literature [12–15]. In addition, the orthogonality relations between guided modes of waveguides, mainly used for microwave applications, have been extensively discussed and applied in the literature [13,16–22]. In this section, we elaborate on some aspects of the modal properties of circular SIFs that have not been adequately explored in the literature; these aspects, however, are crucial to the implementation of the mode expansion approach in computer procedures. A suitable orthogonality relation is identified for the guided modes described in this section and is validated both analytically and numerically. It is worth noting that the radiating eigenmodes of SIFs are not important for MMI-based applications [2] and therefore are not discussed in this section.

A. Modal Properties of Circular Step-Index Fibers

For a circular SIF with a core of refractive index n_1 and radius a, and a cladding with refractive index n_2, the electric and magnetic (EM) field of a guided mode propagating along the z axis can be expressed as [15]

$$\vec{E}(r,\phi,z,t) = \vec{E}(r)\exp(il\phi)\exp[i(\omega t - \beta z)], \tag{1a}$$

$$\vec{H}(r,\phi,z,t) = \vec{H}(r)\exp(il\phi)\exp[i(\omega t - \beta z)], \tag{1b}$$

where ω is the angular frequency of the field; β is the propagation constant; and l is a nonnegative integer denoting the angular dependence of the mode. Based on Maxwell's equations and the boundary conditions at the interface between the core and the cladding, the propagation constant β must satisfy the characteristic equation [15] of

$$\frac{J_{l+1}(ha)}{haJ_l(ha)} = \frac{n_1^2 + n_2^2}{2n_1^2}\frac{K_l'(qa)}{qaK_l(qa)} + \left(\frac{l}{(ha)^2} - R\right), \tag{2a}$$

for EH modes (or TE modes when l equals zero), or that of

$$\frac{J_{l-1}(ha)}{haJ_l(ha)} = -\frac{n_1^2 + n_2^2}{2n_1^2}\frac{K_l'(qa)}{qaK_l(qa)} + \left(\frac{l}{(ha)^2} - R\right), \tag{2b}$$

for HE modes (or TM modes when l equals zero), where J is a Bessel function of the first kind, K is a modified

Bessel function of the second kind,

$$R = \left[\left(\frac{n_1^2 - n_2^2}{2n_1^2} \right)^2 \left(\frac{K_l'(qa)}{qaK_l(qa)} \right)^2 + \left(\frac{l\beta}{n_1 k_0} \right)^2 \left(\frac{1}{(qa)^2} + \frac{1}{(ha)^2} \right) \right]^{1/2}, \tag{2c}$$

$$h^2 = n_1^2 k_0^2 - \beta^2, \quad q^2 = \beta^2 - n_2^2 k_0^2, \tag{2d}$$

$$V^2 = (ha)^2 + (qa)^2 = (n_1^2 - n_2^2) k_0^2 a^2, \tag{2e}$$

where k_0 is the wavenumber of the light in free space, V is the V parameter of the SIF, and ha and qa are within the range of $(0, V)$. The EM field of the guided mode with propagation constant β is described by Eqs. (3.2-6) to (3.2-9) and Eq. (3.2-12) in [15].

The discussion indicates that the propagation constant β is a key parameter for guided modes of an SIF; once β is determined, the EM field can be readily computed. To systematically solve Eqs. (2a) and (2b) for the propagation constants of guided modes of angular order l with a numerical procedure, it is important to investigate the properties of Eqs. (2a)–(2c) and thus determine proper boundary conditions required by the numerical procedure. Note that as ha increases from zero to the V parameter of the fiber, the left side of Eq. (2a) or Eq. (2b) resembles the tangent or cotangent function, with the singularities of the left side occurring at ha that satisfies the equation of $J_l(ha) = 0$; the property of the right side of Eq. (2a) or Eq. (2b), however, is very complicated, except that the right side is a smooth function of ha (or qa). In Appendix A, the properties of the right-hand sides (RHSs) of Eqs. (2a) and (2b) are examined in detail and the results can be summarized as follows:

1. For TE, TM, or EH modes, i.e., $l = 0$ in Eq. (2a) or Eq. (2b), or $l > 0$ in Eq. (2a), the RHS of Eq. (2a) or Eq. (2b) is negative for ha between 0 and the V parameter of the fiber. The RHS has a finite negative value when ha equals 0 and goes to negative infinity when ha approaches V.
2. For HE modes, i.e., $l > 0$ in Eq. (2b), the RHS of Eq. (2b) is positive for ha between 0 and V and has a finite positive value when ha is equal to 0. As ha approaches V, the RHS is expressed as

$$\lim_{ha \to V} \mathrm{RHS}_{\mathrm{HE}}(ha) = +\infty \quad \text{for } l = 1, \tag{3a}$$

$$\lim_{ha \to V} \mathrm{RHS}_{\mathrm{HE}}(ha) = \frac{1}{l-1} \frac{n_2^2}{n_1^2 + n_2^2} \quad \text{for } l > 1. \tag{3b}$$

Based on the properties of Eqs. (2a) and (2b) discussed previously, the cutoff values of the V parameter for guided modes of SIFs can be easily obtained with the graphic approach [13,15]. For example for HE_{1m} modes, the cutoff values V_m satisfy

$$J_1(V_m) = 0, \quad V_1 = 0, \tag{4}$$

where m is a positive integer, indicating that there is no cutoff for HE_{11} modes. For the HE_{lm} mode with l greater than 1, V_m satisfies the equation of

$$\frac{J_{l-1}(V_m)}{V_m J_l(V_m)} = \frac{1}{l-1} \frac{n_2^2}{n_1^2 + n_2^2}, \quad V_m \neq 0, \tag{5}$$

which can be obtained intuitively with the graphic approach [13,15] and is equivalent to Eq. (24) in [12]. Note that the cut-off conditions for TE, TM, EH, and HE_{1m} modes are only dependent on the V parameter of the fiber, while the appearance of an HE_{lm} mode with l greater than 1 is also dependent on the refractive indices of the core and cladding of the SIF.

With the properties of the characteristic Eqs. (2a) and (2b), the number of guided modes and the corresponding propagation constants can be systematically and accurately determined for a given SIF by numerical procedures. It is suggested that the propagation constant β of a guided mode can be used to fully determine the EM field of the mode based on Eqs. (3.2-6)–(3.2-9) and Eq. (3.2-12) in [15]. In the current paper, these equations are rewritten to a set of simplified formulas for the EM field of a guided mode that can be readily implemented in computer procedures. For EH, HE, and TM modes of a SIF, the parameter P defined in Eq. (16) of [12], i.e.,

$$P = l \left(\frac{1}{q^2 a^2} + \frac{1}{h^2 a^2} \right) \left(\frac{J_l'(ha)}{haJ_l(ha)} + \frac{K_l'(qa)}{qaK_l(qa)} \right)^{-1} \tag{6}$$

is adopted and the EM field of the mode with propagation constant β can be expressed as the following:

1. in the core, i.e., $r < a$,

$$E_r(r, \phi) = -\frac{i\beta}{2h} A[(1-P)J_{l-1}(hr) - (1+P)J_{l+1}(hr)]\exp(il\phi), \tag{7a}$$

$$E_\phi(r, \phi) = \frac{\beta}{2h} A[(1-P)J_{l-1}(hr) + (1+P)J_{l+1}(hr)]\exp(il\phi), \tag{7b}$$

$$E_z(r, \phi) = AJ_l(hr)\exp(il\phi), \tag{7c}$$

$$H_r(r, \phi) = \frac{\omega\varepsilon_1}{2h} A[(f_1 P - 1)J_{l-1}(hr) - (f_1 P + 1)J_{l+1}(hr)]\exp(il\phi), \tag{7d}$$

$$H_\phi(r, \phi) = \frac{i\omega\varepsilon_1}{2h} A[(f_1 P - 1)J_{l-1}(hr) + (f_1 P + 1)J_{l+1}(hr)]\exp(il\phi), \tag{7e}$$

$$H_z(r, \phi) = \frac{i\omega\varepsilon_1}{\beta} A f_1 P J_l(hr)\exp(il\phi), \tag{7f}$$

where A is a scalable coefficient, $\varepsilon_1 = \varepsilon_0 n_1^2$, and

$$f_1 = \beta^2/(n_1^2 k_0^2); \tag{7g}$$

2. in the cladding (i.e., $r > a$),

$$E_r(r,\phi) = -\frac{i\beta}{2q}C[(1-P)K_{l-1}(qr) + (1+P)K_{l+1}(qr)]\exp(il\phi), \tag{8a}$$

$$E_\phi(r,\phi) = \frac{\beta}{2q}C[(1-P)K_{l-1}(qr) - (1+P)K_{l+1}(qr)]\exp(il\phi), \tag{8b}$$

$$E_z(r,\phi) = CK_l(qr)\exp(il\phi), \tag{8c}$$

$$H_r(r,\phi) = -\frac{\omega\varepsilon_2}{2q}C[(1-f_2P)K_{l-1}(qr) - (1+f_2P)K_{l+1}(qr)]\exp(il\phi), \tag{8d}$$

$$H_\phi(r,\phi) = -\frac{i\omega\varepsilon_2}{2q}C[(1-f_2P)K_{l-1}(qr) + (1+f_2P)K_{l+1}(qr)]\exp(il\phi), \tag{8e}$$

$$H_z(r,\phi) = \frac{i\omega\varepsilon_2}{\beta}Cf_2PK_l(qr)\exp(il\phi), \tag{8f}$$

where $\varepsilon_2=\varepsilon_0 n_2^2$,

$$C = AJ_l(ha)/K_l(qa), \tag{8g}$$

$$f_2 = \beta^2/(n_2^2k_0^2). \tag{8h}$$

The complete description of the EM field of the guided mode is obtained by multiplying Eqs. (7a)–(7f) and (8a)–(8f) by the t and z dependence of $\exp[i(\omega t-\beta z)]$. Note that for TM modes, l is zero and hence P is zero. It can be verified from Eqs. (7a)–(7f) and (8a)–(8f) that the field components H_r, H_z, and E_φ are zero for TM modes. For TE modes, $J_0'(ha)/[haJ_0(ha)]+K_0'(qa)/[qaK_0(qa)]=0$, so the parameter P is not defined by Eq. (6); therefore, Eqs. (7a)–(7g) and (8a)–(8h) are not applicable in this case. The EM field of a TE mode with propagation constant β can be derived as follows:

1. in the core,

$$E_\phi(r,\phi) = -\frac{i\beta}{h}AJ_1(hr), \tag{9a}$$

$$H_r(r,\phi) = i\frac{\omega\varepsilon_0\beta^2}{hk_0^2}AJ_1(hr), \tag{9b}$$

$$H_z(r,\phi) = \frac{\omega\varepsilon_0\beta}{k_0^2}AJ_0(hr), \tag{9c}$$

2. in the cladding,

$$E_\phi(r,\phi) = \frac{i\beta}{q}A\frac{J_0(ha)}{K_0(qa)}K_1(qr), \tag{10a}$$

$$H_r(r,\phi) = -\frac{i\omega\varepsilon_0\beta^2}{qk_0^2}A\frac{J_0(ha)}{K_0(qa)}K_1(qr), \tag{10b}$$

$$H_z(r,\phi) = \frac{\omega\varepsilon_0\beta}{k_0^2}A\frac{J_0(ha)}{K_0(qa)}K_0(qr), \tag{10c}$$

all the other components of the EM field of the TE mode, namely, E_r, E_z, and H_φ, are zero.

In the previous discussion, the guided modes are considered having an angular dependence of $\exp(+il\phi)$. Reference [15] briefly mentioned that for $l>0$, the angular dependence of $\exp(-il\phi)$ in Eqs. (1a) and (1b) corresponds to an independent set of eigenmodes for a given SIF; therefore, $+l$ and $-l$ modes together constitute the full set of the guided modes for the mode expansion approach. For modes propagating in $+z$ direction, the electric fields of $+l$ and $-l$ modes can be expressed as

$$\vec{E}^{(+l)}(r,\phi) = \vec{E}(r,\phi;l) = \vec{E}^{(l)}(r)\exp(il\phi), \tag{11a}$$

$$\vec{E}^{(-l)}(r,\phi) = \vec{E}(r,\phi;-l) = \vec{E}^{(-l)}(r)\exp(-il\phi). \tag{11b}$$

Similar expressions can be derived for the magnetic fields. With Maxwell's curl equations of Eqs. (3.1-3a)–(3.1-4c) in [15], it can be verified that if an EM field of $E_r(r,\varphi;l)$, $E_\varphi(r,\varphi;l)$, $E_z(r,\varphi;l)$, $H_r(r,\varphi;l)$, $H_\varphi(r,\varphi;l)$, and $H_z(r,\varphi;l)$ is a solution to the Maxwell's curl equations, so is the EM field of $E_r^*(r,\varphi;l)$, $E_\varphi^*(r,\varphi;l)$, $-E_z^*(r,\varphi;l)$, $H_r^*(r,\varphi;l)$, $H_\varphi^*(r,\varphi;l)$, and $-H_z^*(r,\varphi;l)$. Therefore, the electric field of $-l$ mode can be obtained directly from the corresponding $+l$mode as follows:

$$E_r^{(-l)}(r) = [E_r^{(l)}(r)]^*, E_\phi^{(-l)}(r) = [E_\phi^{(l)}(r)]^*, E_z^{(-l)}(r) = -[E_z^{(l)}(r)]^*, \tag{12}$$

and the magnetic field can be determined in a similar way. Since a $-l$ mode has the same propagation constant as the corresponding $+l$ mode, these two modes are degenerate. The complex amplitudes of the transverse components of the electric fields of the $-l$ and $+l$ modes further indicate that left-hand (LH) polarization and right-hand (RH) polarization can be associated with these two modes, respectively [13]. Thus, the $-l$ and $+l$ modes, with different polarization states, are degenerate. Due to the degeneracy, any linear combination of the $-l$ and $+l$ modes is an eigenmode with the same propagation constant of β. For weakly guiding SIFs, the double degenerate LP modes LP_{0m} [23] can be derived using HE_{1m} and HE_{-1m} modes. Additionally, the discussion on $-l$ modes allows for the understanding of the fourfold degeneracy of the LP_{lm} modes with l greater than 0 [23]. The four independent LP_{1m} modes can be obtained with linear superposition of the two degenerate modes HE_{2m} and HE_{-2m} and the two additional modes TE_{0m} and TM_{0m}. It needs to be clarified that there is not another mode that is degenerate with a TE_{0m} or TM_{0m} mode. For LP_{lm} modes with l greater than 1, the modes $EH_{l+1,m}$ and $EH_{-(l+1),m}$ modes are degenerate with the modes $HE_{l-1,m}$ and $HE_{-(l-1),m}$; thus, the degeneracy of LP_{lm} modes is fourfold.

According to this discussion, a complete set of guided modes of a circular SIF can be described as follows, (1) for

$l=0$, the guided modes are TE_{0m} and TM_{0n} modes, and each of them is nondegenerate; and (2) for $l>0$, the guided modes are $HE_{\pm l,m}$ and $EH_{\pm l,n}$ modes, and each mode with $+l$ has a degenerate counterpart with $-l$ that has the same propagation constant. It is noteworthy that since any linear superposition of two degenerate eigenmodes is an eigenmode, other complete sets of guided modes can be derived from the set of modes described above.

B. Mode Orthogonality Relation

With the modal properties of SIFs described in Subsection 2.A, the complete set of the guided modes can be computed for a given SIF, forming a Hilbert space where an arbitrary propagating field in the fiber can be expanded as a linear superposition of the guided modes of the SIF. To facilitate mode expansion of an EM field in an SIF, it is important to adopt a suitable orthogonality relation between the guided modes of the fiber.

The orthogonality relations presented in the literature are mainly derived for waveguides with closed transverse boundaries in microwave applications, where the transverse boundaries are perfectly electric or magnetic, or subject to the impedance boundary condition [16–22]. The Lorentz reciprocal principle or its generalized version for anisotropic materials is applied in [16,17,19,21,22] to the normal modes of waveguides (and those of the complementary waveguides if waveguides are nonreciprocal) [22] to derive the orthogonality relations. In [18,20], Maxwell curl equations for the normal modes of waveguides are expressed in terms of linear operators, and the spectral theory of linear operators is utilized to obtain the orthogonality properties of the eigenvectors of the linear operators (i.e., the normal modes of the waveguides). The two approaches have yielded the same orthogonality relations. For a bidirectional waveguide whose normal modes are in the form [16] of

$$\bar{E}^{(n)}(x,y,z,t) = (\vec{e}_T^{(n)}(x,y) + \hat{z}e_z^{(n)}(x,y))\exp(-\gamma_n z)\exp(i\omega t), \tag{13}$$

where the subscript T denotes the transverse component, the orthogonality relation between the modes can be expressed as

$$\iint_S \mathrm{d}s\hat{z}\cdot(\vec{e}_T^{(n)}\times\vec{h}_T^{(m)}) = N_n\delta_{mn}, \tag{14}$$

where the integration is over the cross section of the closed boundary waveguide, N_n is the normalization constant, and δ_{mn} is the Kronecker delta. It is worth noting that the orthogonality relation in Eq. (14) is valid for lossy, amplifying, or lossless waveguides. If the waveguide is lossless, γ_n in Eq. (13) becomes purely imaginary and a similar orthogonality relation,

$$\iint_S \mathrm{d}s\hat{z}\cdot(\vec{e}_T^{(n)}\times\vec{h}_T^{(m)^*}) = 2P_n\delta_{mn} \tag{15}$$

can be derived, where the superscript * denotes the complex conjugate. Equation (15) is known as the power orthogonality relation [16], meaning that in a lossless uniform waveguide, the powers of individual modes propagate independently in the waveguide.

Although it is mentioned in [18,22] that the orthogonality relations derived for closed boundary waveguides are applicable to open boundary waveguides such as optical fibers, no details are provided to justify the statement. For an SIF, the dielectric function is discontinuous at the material interface and thus can play an important role in the orthogonality properties of the guided modes. With the material interfaces in fibers taken into account, the Lorentz reciprocal theorem is applied in Appendix B to derive the orthogonality relations for the guided modes of bidirectional optical fibers with discontinuous dielectric functions. It is demonstrated that the guided modes of bidirectional optical fibers satisfy an almost identical orthogonality relation to Eq. (14) [or Eq. (15) for a lossless fiber], except that for optical fibers, the domain of integration in Eq. (14) [or Eq. (15)] is the entire two-dimensional plane.

For optical fibers with a weak guidance approximation, the guided modes can be considered as linearly polarized, or equivalently scalar, and the orthogonality relations in Eqs. (14) and (15) can be simplified to

$$\iint_S \mathrm{d}s\vec{e}_T^{(n)}\cdot\vec{e}_T^{(m)} = M_n\delta_{mn}, \tag{16}$$

$$\iint_S \mathrm{d}s\vec{e}_T^{(n)}\cdot\vec{e}_T^{(m)^*} = Q_n\delta_{mn}, \tag{17}$$

respectively [23]. The orthogonality relation in Eq. (15), denoted as OR I, and that in Eq. (17), denoted as OR II, are applied to the guided modes of a circular coreless fiber with a 200 μm diameter core of the refractive index of 1.565 and a cladding of air. The normalized orthogonality coefficient N_{mn} between modes m and n are calculated with OR I and OR II to demonstrate the validity of the two orthogonality relations. The coefficient N_{mn} is defined as

$$N_{mn} = P_{mn}/[P_{mm}P_{nn}]^{1/2}, \tag{18}$$

where P_{mn} is

$$P_{mn}^{(I)} = \iint_S \mathrm{d}s\hat{z}\cdot(\vec{e}_T^{(m)}\times\vec{h}_T^{(n)^*}), \tag{19a}$$

for OR I, or

$$P_{mn}^{(II)} = \iint_S \mathrm{d}s\vec{e}_T^{(m)}\cdot\vec{e}_T^{(n)^*} \tag{19b}$$

for OR II. The guided modes of the fiber are computed for the wavelength of 1.535 μm; then, the normalized orthogonality coefficient between two guided modes is computed with highly accurate numerical schemes. Since two guided modes with different angular orders satisfy Eqs. (15) and (17) automatically, a set of HE and EH modes with the same angular order is used to calculate the normalized orthogonality coefficients for OR I and OR II in double precision, and the results are listed in Tables 1 and 2, respectively. It can be observed that the normalized orthogonality coefficient matrix in Table 1 has negligibly small off-diagonal elements, implying that OR I is a suit-

Table 1. Normalized Orthogonality Coefficients N_{mn} Based on OR I

	$HE_{18,21}$	$HE_{18,22}$	$EH_{18,21}$	$EH_{18,22}$
$HE_{18,21}$	1.00	9.87×10^{-12}	-9.00×10^{-13}	-2.26×10^{-12}
$HE_{18,22}$	9.86×10^{-12}	1.00	-7.33×10^{-13}	-3.47×10^{-12}
$EH_{18,21}$	-9.97×10^{-13}	-9.00×10^{-13}	1.00	5.38×10^{-13}
$EH_{18,22}$	-2.46×10^{-12}	-3.76×10^{-12}	5.39×10^{-13}	1.00

able orthogonality relation for the guided modes of the SIF considered. The coefficient matrix in Table 2, however, has relatively large off-diagonal entries, denoting that OR II is not valid in this case. The two orthogonality relations have been extensively tested for other guided modes of the 200 μm core fiber; the results consistently show that OR I is well satisfied, while OR II does not hold well. Therefore, OR I is adopted for the mode expansion approach in this study.

3. AN ADAPTIVE ALGORITHM FOR THE MODE EXPANSION APPROACH

According to the normal mode theory [23], a propagating field inside an SIF can be expressed as a superposition of the guided modes of the fiber, i.e.,

$$\vec{E}(r,\phi,z)=\sum_{n=1}^{N}C_n\vec{E}^{(n)}(r,\phi,z)=\sum_{n=1}^{N}C_n\vec{e}^{(n)}(r,\phi)\exp(-i\beta_n z), \tag{20}$$

where N is the number of the guided modes and $\vec{E}^{(n)}$ is the electric field of mode n. This superposition (with the same coefficients) also applies to the magnetic field in the fiber. With the orthogonality relation as defined in Eq. (15), the coefficient C_n can be determined as follows:

$$C_n=\frac{\iint_S \mathrm{d}s\hat{z}\cdot[\vec{E}_T^{in}(r,\phi,z=0)\times\vec{h}_T^{(n)^*}(r,\phi)]}{\iint_S \mathrm{d}s\hat{z}\cdot(\vec{e}_T^{(n)}(r,\phi)\times\vec{h}_T^{(n)^*}(r,\phi))}, \tag{21}$$

where the domain of integration S is the transverse plane and $\vec{E}^{in}$ is the field incident on the fiber. Once the coefficients of the guided modes are determined, the field along the entire fiber is known from Eq. (20). Therefore, to study the MMI of a field in a multimode SIF with the mode expansion approach, the first step is to perform mode expansion of the incident field described by Eq. (21).

For an MMF used as an MMI component, it is necessary that a number of guided modes are supported by the fiber. For example, the outer diameter (OD) 200 μm coreless fiber as described in [6] allows for more than 10^5 guided modes. Given the high mode density in such MMFs, it is impractical to directly implement the mode expansion described in Eqs. (20) and (21) in numerical procedures. A more efficient algorithm to perform the mode expansion is to first identify a small subset of the guided modes of an MMF according to the incident field and then expand the field based on these guided modes. More specifically, the algorithm must be capable of adaptively determining a proper subset of the guided modes for expanding a given incident field. This is feasible, as the guided modes of a fiber generally are not equally excited by an incident field; some modes are strongly excited and carry more power, while others are weakly excited. Therefore, in an adaptive algorithm, a proper subset of guided modes for an incident field can be defined to consist of those strongly excited guided modes. To systematically identify a subset of guided modes for a given incident field, it is important to simplify the representation of the incident field and accordingly adopt a complete set of guided modes defined in a suitable form.

Table 2. Normalized Orthogonality Coefficients N_{mn} Based on OR II

	$HE_{18,21}$	$HE_{18,22}$	$EH_{18,21}$	$EH_{18,22}$
$HE_{18,21}$	1.00	-3.86×10^{-5}	-1.48×10^{-3}	7.11×10^{-4}
$HE_{18,22}$	-3.86×10^{-5}	1.00	-9.97×10^{-3}	-1.53×10^{-3}
$EH_{18,21}$	-1.48×10^{-3}	-9.97×10^{-3}	1.00	-2.86×10^{-5}
$EH_{18,22}$	7.11×10^{-4}	-1.53×10^{-3}	-2.86×10^{-5}	1.00

Given the circular symmetry of multimode SIFs considered in this study, the transverse components of an arbitrary incident field can be expanded in Fourier series as follows:

$$\vec{E}_T^{in}(r,\phi,z=0)=\sum_{l=-L}^{L}\vec{e}_T^{in}(r;l)\exp(il\phi), \tag{22a}$$

$$\vec{H}_T^{in}(r,\phi,z=0)=\sum_{l=-L}^{L}\vec{h}_T^{in}(r;l)\exp(il\phi), \tag{22b}$$

where L is the Fourier order corresponding to the highest spatial frequency of the incident field in the angular direction. It is evident that fast Fourier transform (FFT) is a natural choice to perform the Fourier series expansions in Eqs. (22a) and (22b) with high efficiency. Based on these expansions, it can be derived that

$$\iint_S \mathrm{d}s\hat{z}\cdot[\vec{E}_T^{in}\times\vec{H}_T^{in^*}]=\sum_{l=-L}^{L}\iint_S \mathrm{d}s\hat{z}\cdot[\vec{e}_T^{in}(r;l)\times\vec{h}_T^{in^*}(r;l)], \tag{23a}$$

$$R_z=\hat{z}\cdot(\vec{E}_T^{in}\times\vec{H}_T^{in^*})/2, \tag{23b}$$

where R_z is the z component of the complex Poynting vector of the incident field. Equations (23a) and (23b) imply that the total power of the incident field in the z direction is the sum of the powers of its Fourier components in the same direction. As a result, the percentage of the power of each Fourier component out of the power of the incident field can be determined systematically, and the set of the Fourier orders carrying most of the power can be identified accordingly. Consequently, a simplified representation of the incident field can be defined using its major Fourier components, i.e.,

$$\vec{E}_T^{in}(r,\phi,z=0) \approx \vec{E}_T^{(s)}(r,\phi,z=0) = \sum_{l\in SL} \vec{e}_T^{in}(r;l)\exp(il\phi), \tag{24}$$

where SL is the subset formed by the major Fourier orders. Note that the difference between the incident field and its approximation can be made desirably small by including more Fourier orders in the subset SL.

It is recognizable that the set of the guided modes described in Section 2, with the orthogonality relation defined in Eq. (15), is a suitable set for the mode expansion approach since (1) modes with ± angular orders fit naturally in the context where the Fourier expansions of Eqs. (22a) and (22b) are used to represent an incident field, and (2) the Fourier component of the incident field with the dependence of $\exp(il\varphi)$ only excites the guided modes with the same angular dependence. Therefore, for the simplified incident field in Eq. (24), the complete set of modes with ± angular orders allows for a suitable subset of the modes to be systematically defined as consisting of the ones with an angular order in subset SL. For example, if the transverse component of an incident field is real and linearly polarized, it is known that in a cylindrical coordinate system, only the $\exp(\pm i\varphi)$ terms are nonzero in the Fourier series expansion of the components of the incident field such as $\vec{E}_r^{in}(r,\phi,z=0)$. Therefore, a suitable subset of the guided modes to expand the incident field can be chosen to consist of modes with angular order ±1, namely, the $HE_{\pm 1,m}$ and $EH_{\pm 1,n}$ modes.

According to the modal properties discussed in Section 2, two integers l (positive or negative) and n_l (positive) can be used as mode numbers to label a guided mode in a circular SIF, where l denotes the mode having an angular dependence of $\exp(il\varphi)$. For example, TE_{0m} and TM_{0n} modes are sorted in the descending order of their propagation constants and are labeled as modes $(0, n_0)$. Similarly, HE_{lm} and EH_{ln} modes are labeled as modes (l, n_l). With this notation for labeling modes, the mode expansion in Eq. (20) can be rewritten as [24]

$$\vec{E}_T(r,\phi,z) = \sum_{l=-L}^{L}\sum_{n_l=1}^{N_l} C_{l,n_l}\vec{e}_T^{(l,n_l)}(r)\exp[i(l\phi-\beta_{l,n_l}z)], \tag{25a}$$

and the expansion coefficient is

$$C_{l,n_l} = \frac{\int_0^\infty r\mathrm{d}r\hat{z}\cdot[\vec{e}_T^{in}(r;l)\times\vec{h}_T^{(l,n_l)^*}(r)]}{\int_0^\infty r\mathrm{d}r\hat{z}\cdot[\vec{e}_T^{(l,n_l)}(r)\times\vec{h}_T^{(l,n_l)^*}(r)]}. \tag{25b}$$

Unlike in Eq. (21), where two-dimensional integrals are involved, only two one-dimensional integrals need to be evaluated in Eq. (25b), indicating that the complexity in calculating the expansion coefficients is greatly reduced. This represents another advantage of using the combination of the Fourier series representation of an incident field and the set of the guided modes described in Section 2.

Based on Eqs. (24), (25a), and (25b), the adaptive algorithm for mode expansion, capable of analyzing MMI in highly MMFs, can be summarized as follows:

1. FFT is employed to obtain the Fourier series expansion of an incident field. The percentage of the power of each Fourier component is determined and used to define a subset of the Fourier components SL that carry a desirable percentage (e.g., 99.9%) of the total incident power, yielding a simplified incident field of Eq. (24).
2. For Fourier order l in subset SL, Eq. (25b) is evaluated to determine the expansion coefficients of the guided modes with angular order l. With the orthogonality properties of the modes, it can be similarly derived that the total power carried by all the modes with angular order l is the sum of the powers of individual modes (l, n_l). As a result, a subset of the guided modes with angular order l, denoted by SN_l, can be defined by neglecting the modes that are weakly excited by the incident field.
3. Step 2 is repeated for each Fourier order in subset SL to obtain the mode expansion of the excited field in the fiber, i.e.,

$$\vec{E}_T(r,\phi,z) \cong \sum_{l\in SL}\sum_{n_l\in SN_l} C_{l,n_l}\vec{e}_T^{(l,n_l)}(r)\exp[i(l\phi-\beta_{l,n_l}z)]. \tag{26}$$

The error induced by using a subset of the guided modes can be reduced to a desirable level by including more modes in the subset.

4. MULTIMODE INTERFERENCE IN FIBERS

With the adaptive algorithm discussed in Section 3, the mode expansion approach can be effectively employed to investigate MMI in highly MMFs. In this section, the new approach is validated with two MMI-based applications: (1) using coreless fiber segments for in-phase supermode selection in MCF lasers [6,7], and (2) applying an SMF-MMF-SMF structure to design a refractometer sensor [4] or a bandpass filter [5].

A. Coreless Fibers for In-Phase Supermode Selection

It has been demonstrated in [6,7] that coreless fibers can be utilized as mode-selection components to build monolithic MCF lasers operating in the in-phase supermode. A coreless fiber can be viewed as an SIF with a large glass core and an air cladding; hence, a large number of modes

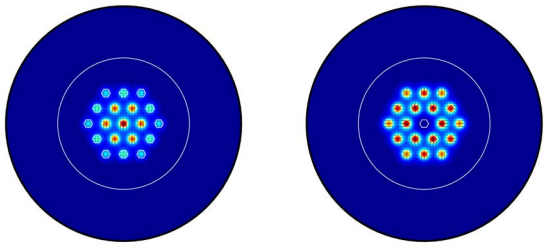

(a) (b)

Fig. 1. (Color online) Two guided supermodes of the 19-core MCF: (a) HE_{11}-like fundamental supermode and (b) TM_{01}-like higher-order supermode.

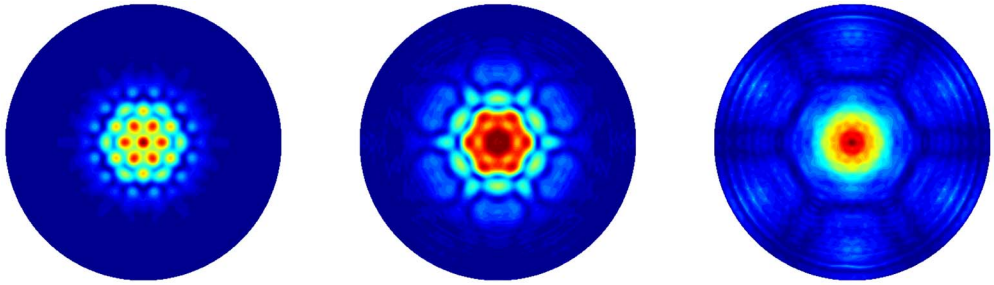

(a) (b) (c)

Fig. 2. (Color online) Amplitude profiles of the field at distances of (a) 300, (b) 500, and (c) 1000 μm along the coreless fiber, respectively. The fundamental supermode shown in Fig. 1(a) is the incident field and the FE-BPM is used to obtain the results.

are guided by the fiber. When a supermode of an MCF is coupled into a coreless fiber, the supermode excites a number of guided modes of the coreless fiber, and therefore is subject to MMI. Different supermodes experience different types of MMI in coreless fibers, leading to the in-phase supermode selection in MCF lasers [7]. To understand the mode-selection properties of a coreless fiber, it is important to simulate MMI or the propagating fields of different supermodes in the coreless fiber.

The 19-core MCF laser in [6] is analyzed to investigate the mode-selection properties of the coreless fiber with an OD of 200 μm. First, a mixed high-order vector finite-element method [25] is employed to compute the guided supermodes of the MCF with high accuracy. Two of the guided supermodes, namely, an HE_{11}-like fundamental supermode and a TM_{01}-like high-order supermode, are illustrated in Figs. 1(a) and 1(b). Each supermode is then coupled into the OD 200 μm coreless fiber, and the propagation of the supermode inside the coreless fiber is simulated to obtain the MMI. For comparison, the mode expansion approach developed in this study and the vectorial FE-BPM [26] are employed to study the propagation of a field along the coreless fiber independently. The Padé approximant operator [27] is implemented in the FE-BPM to allow for wide-angle beam propagation. Using the fundamental supermode in Fig. 1(a) as the incident field, the amplitude profiles of the electric field at various locations along the coreless fiber are determined with the two approaches and are illustrated in Figs. 2(a)–2(c) and Figs. 3(a)–3(c), respectively. The similarity between the amplitude profiles from the two different approaches implies that the mode expansion approach properly simulates the field propagation in the coreless fiber. A careful examination of Figs. 2(a)–2(c) shows that as the propagation distance increases, the amplitude profiles obtained with the FE-BPM become noisy and start to lose symmetry. This is due to the fact that for the BPM, the numerical error accumulates with the propagation distance and contaminates the physical field in the coreless fiber. In the case of the mode expansion approach, the amplitude profiles shown in Figs. 3(a)–3(c) are clear and preserve the symmetry at all three distances. The reason is that for the mode expansion approach, the numerical error is introduced only by neglecting the weakly excited modes, and hence does not increase with the propagation distance. The simulation with the mode expansion approach shows that for the fundamental supermode, more than 99.8% of its total power is coupled to fewer than 220 guided modes of the coreless fiber, which are used to form the mode expansion and generate the results in Figs. 3(a)–3(c). It is also known that the computational cost for the BPM is proportional to the propagation distance, while for the mode expansion approach, the cost is fixed. Based on these facts, the mode expansion approach is preferable to the FE-BPM in cases where field propagation over a substantial distance is required.

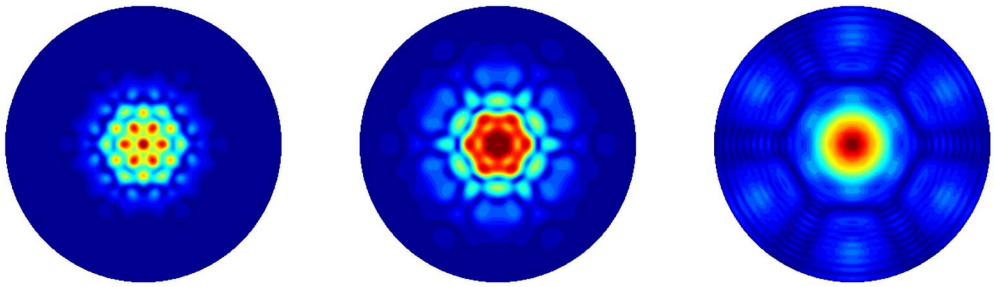

(a) (b) (c)

Fig. 3. (Color online) Amplitude profiles of the field at distances of (a) 300, (b) 500, and (c) 1000 μm along the coreless fiber, respectively. The fundamental supermode shown in Fig. 1(a) is the incident field and the mode expansion approach is employed here.

The self-imaging properties of a field along a coreless fiber, due to MMI, can be quantified by an effective amplitude reflection coefficient γ [28], which is redefined here in vectorial form as

$$\gamma(z) = \frac{\iint_S ds\hat{z} \cdot [\vec{E}_T(r,\phi,z) \times \vec{H}_T^*(r,\phi,z=0)]}{\iint_S ds\hat{z} \cdot [\vec{E}_T(r,\phi,z=0) \times \vec{H}_T^*(r,\phi,z=0)]}. \quad (27)$$

With Eq. (26) and the mode orthogonality relation, Eq. (27) can be rewritten as

$$\gamma(z) = \left| \sum_{l \in SL} \sum_{n_l \in SN_l} |C_{l,n_l}|^2 P^{(l,n_l)} \exp(-i\beta_{l,n_l} z) \right| \Big/ TP, \quad (28a)$$

$$TP = \sum_{l \in SL} \sum_{n_l \in SN_l} |C_{l,n_l}|^2 P^{(l,n_l)}, \quad (28b)$$

$$P^{(l,n_l)} = \int_0^\infty r dr \hat{z} \cdot [\vec{e}_T^{(l,n_l)}(r) \times \vec{h}_T^{(l,n_l)^*}(r)]. \quad (28c)$$

The coefficients γ of the fundamental supermode in Fig. 1(a) and the higher-order supermode in Fig. 1(b) are calculated as functions of the propagation distance z along the coreless fiber and are shown in Figs. 4(a) and 4(b), respectively. To compare the self-imaging properties of a supermode in a coreless fiber with those in a Talbot cavity [28–30], the two supermodes are also propagated in a bulk medium (i.e., a Talbot cavity) with the same refractive index as that of the coreless fiber. The corresponding coefficients γ are calculated with the vectorial diffraction theory and are illustrated in Figs. 4(a) and 4(b) with dashed black curves. For each supermode, the results show that when the propagation distance is less than a critical value, the self-imaging properties of the supermode in the coreless fiber are the same as those in the Talbot cavity. This is physically consistent since a supermode can be considered as being composed of spatially distributed beams, with each beam located at a corresponding core of the MCF laser. If each beam propagates a short distance, the diffracted beam is inside the lateral boundary of the coreless fiber, implying that the propagation of the beam in the coreless fiber is not affected by the lateral boundary of the fiber; therefore, it is the same as that in the bulk medium. When the propagation distance exceeds the critical value, the self-imaging properties of the supermode in the coreless fiber start to deviate from those in the Talbot cavity. This is due to the fact the diffracted beams in a supermode are larger than the lateral size of the coreless fiber, causing the propagated field of the supermode in the coreless fiber to be different from that in the bulk medium.

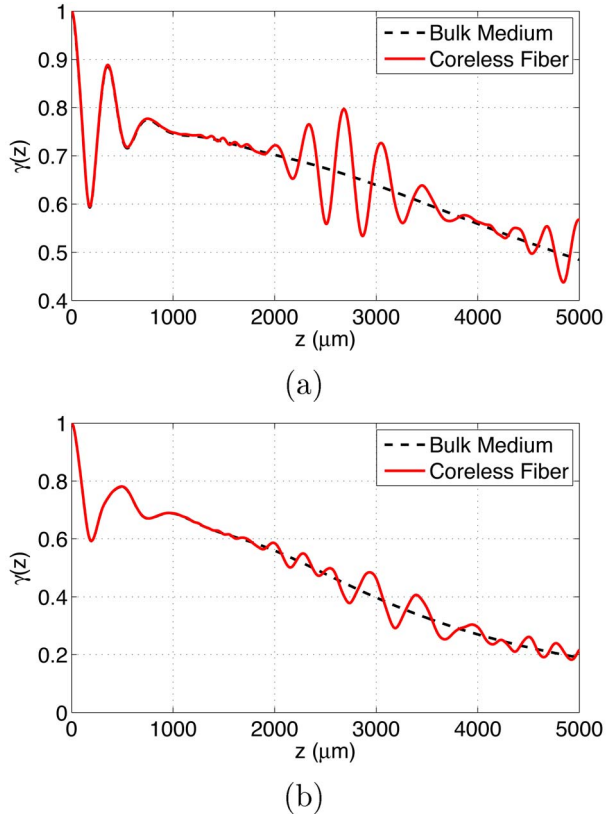

Fig. 4. (Color online) Effective amplitude reflection coefficient γ of (a) fundamental supermode in Fig. 1(a) or (b) higher-order supermode in Fig. 1(b) as a function of the propagation distance z along the OD 200 μm coreless fiber or a bulk medium of the same refractive index as that of the coreless fiber, respectively.

In [7], the effective amplitude reflection coefficients γ of all guided supermodes are calculated with the mode expansion approach to investigate the mode-selection properties of the OD 200 μm coreless fiber segment in a 19-core MCF laser. Based on the coefficients γ, it is predicted that in the MCF laser, the in-phase supermode selection can only be achieved with the coreless fiber segment within a certain length range. If the coreless fiber is longer than a critical value, the in-phase supermode selection cannot be realized. The experimental results in [7] show that the in-phase supermode selection is obtained for the MCF laser with a coreless fiber segment of 1660 μm (i.e., the equivalent propagation distance z along the coreless fiber is 3320 μm). When a coreless fiber with a longer length of 3380 μm (i.e., z is 6760 μm) is utilized in the MCF laser, the beam quality of the laser deteriorates and the MCF laser is not operating in the in-phase supermodes. To investigate how the numerical simulations compare with the experimental results, the coefficients γ of all guided supermodes at the propagation distances of 3320 and 6760 μm are illustrated in Fig. 5. As it is shown, the two in-phase supermodes have the largest

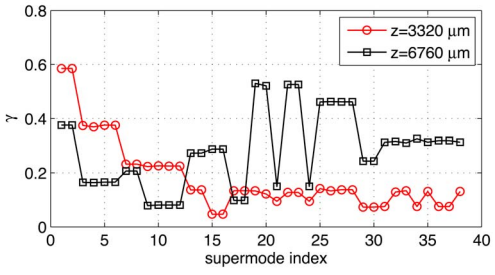

Fig. 5. (Color online) Coefficients γ of all guided supermodes of the MCF laser at the propagation distances of 3320 and 6760 μm along the coreless fiber segment.

coefficients γ among all guided supermodes at 3320 μm, indicating that the in-phase supermodes are favored by the MCF laser. However, at 6760 μm, eight high-order guided supermodes have larger coefficients γ than the in-phase supermodes, with high-order modes favored by the MCF laser. This indicates that the numerical prediction is in good agreement with the experiment data. In the case of a Talbot cavity, numerical simulations show that for the MCF laser, the in-phase supermodes are favored as long as the cavity length is beyond a critical value (see similar results in [29,30]). Therefore, it can be concluded that for long cavity length, the physical mechanism for the mode selection with a coreless fiber is dominated by the MMI effect and is fundamentally different from that utilizing a Talbot cavity.

B. Self-Imaging in a Multimode Fiber

In [4,5], the MMI and self-imaging of optical fields in the MMF segment of an SMF-MMF-SMF structure is utilized to design an all-fiber refractometer sensor and an all-fiber bandpass filter, respectively. Although the numerical schemes employed in [4,5] to obtain the optimum designs are suitable for the designs with circular symmetry, they are not applicable to studying the effect of a misalignment between the SMF and MMF segments. In this section, the mode expansion approach developed in Section 3 is applied to analyze the effect of a misalignment on the self-imaging in an MMF segment.

In the SMF-MMF-SMF structure studied here, the Corning SMF-28 is used as the input and output SMFs and a coreless fiber with an outer diameter of 62.5 μm is used for the MMF. The refractive indices of the core and the cladding, denoted by n_{core} and n_{clad}, and the core radius a_{core} of each fiber are listed in Table 3. It is assumed that the field propagating along the input SMF is the HE_{11} mode of the fiber with its transverse component of the electric field linearly polarized in the vertical (or y) direction, as illustrated in Fig. 6(a). As a reference case, the centers of the SMF and MMF segments are considered as being perfectly aligned, and the mode expansion approach is employed to calculate the coefficient γ of the field in the MMF segment as a function of distance z along the MMF, as illustrated by the solid black curves in Figs. 7(a) and 7(b). The computed $\gamma(z)$ shows that the first self-imaging position of the HE_{11} mode incident on the MMF is at the distance of 58.412 mm along the MMF, where the coefficient γ has a maximum value of 93%. It can be easily derived that the coupling efficiency η in Eq. (3) of [5] equals γ^2, yielding a coupling efficiency of 86% for an MMF segment of 58.412 mm. Note that the amplitude of the electric field at the self-imaging position, as illustrated in Fig. 6(b), is not circularly symmetric. This is due to the fact that the field coupled into the MMF segment is linearly polarized in the vertical direction and, therefore, experiences noncircularly symmetric Fresnel reflection at the interface between the core and cladding of the MMF, leading to the break of the circular symmetry in the amplitude of the field. It is clear that the polarization effect shown in Fig. 6(b) cannot be obtained with the scalar approaches in [4,5], where the field in the MMF is always circularly symmetric.

Table 3. Parameters for the SMF-MMF-SMF Structure at the Wavelength of 1.55 μm

	n_{core}	n_{clad}	a_{core} (μm)
SMF[31,32]	1.44924	1.44402	4.2
MMF	1.44402	1.0	62.5

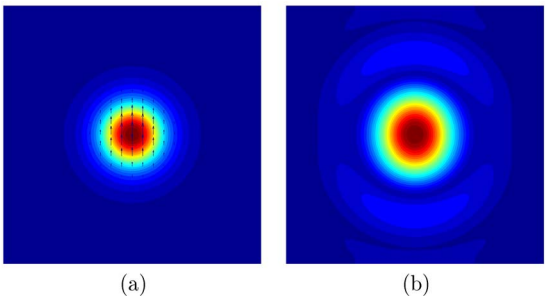

Fig. 6. (Color online) (a) HE_{11} mode of the SMF segment of the SMF-MMF-SMF structure and (b) the amplitude of the field at the self-imaging position along the MMF segment of the perfectly aligned SMF-MMF-SMF structure.

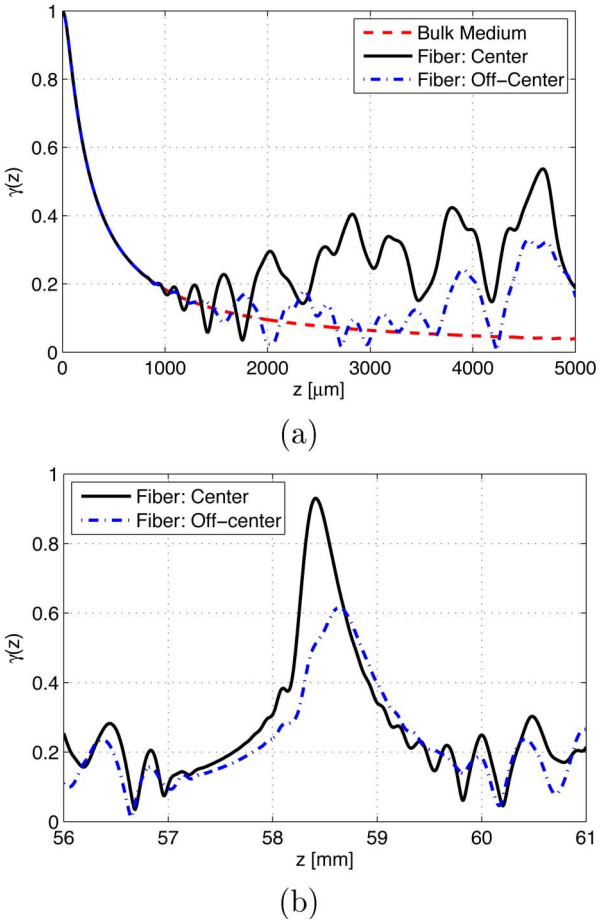

Fig. 7. (Color online) Coefficient γ of the field in the MMF segment of the SMF-MMF-SMF structure as a function of the propagation distance z. The solid curves are for the perfectly aligned structure, and the dash-dot curves are for the misaligned structure. The dashed curve corresponds to the coefficient γ of the field in a bulk medium of the same refractive index as that of the MMF core.

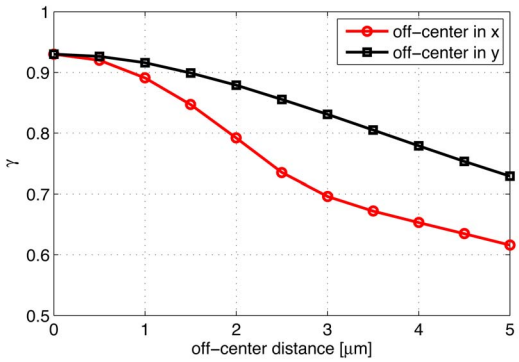

Fig. 8. (Color online) Coefficient γ at the self-imaging position as a function of the offset between the centers of the input SMF and MMF segments.

The effect of a misalignment between the SMF and MMF segments is studied by analyzing a misaligned structure where the centers of the SMFs are shifted by 5 μm with respect to the center of the MMF in the horizontal (or x) direction. The coefficient γ of the field in the MMF segment is similarly calculated and illustrated by the dash-dot blue curves in Figs. 7(a) and 7(b). For comparison, the HE_{11} mode in Fig. 6(a) is also propagated in a bulk medium of the same refractive index as the MMF, and the coefficient γ of the field in the bulk medium is calculated with the vectorial diffraction theory and is shown by the dashed red curve in Fig. 7(a). Similar to Figs. 4(a) and 4(b), the perfect overlap among the lines of the three different structures at short propagation distances indicates that the results obtained from the mode expansion approach are physically consistent and intelligible. It can be observed that when the propagation distance is beyond a critical value, the coefficient γ for the misaligned structure deviates from that for the aligned structure. Although a small misalignment between the SMF and MMF segments shifts the self-imaging position by a relatively small amount, as shown in Fig. 7(b), the maximum coefficient γ, occurring at the self-imaging position, is greatly reduced.

To further demonstrate the polarization effect on MMI in the MMF segment of a misaligned structure, the center of the input SMF segment is shifted away from the center of the MMF in either the horizontal (x) direction or the vertical (y) direction. In each case, the coefficient γ at the self-imaging position is calculated as a function of the offset between the centers of the input SMF and MMF segments and is shown in Fig. 8. The figure shows that for the same amount of misalignment in the range considered, better self-imaging is always obtained for the y-misaligned structure than the x-misaligned structure. It is clear that this polarization effect on MMI has to be resolved with vectorial approaches.

Based on the two examples presented in this subsection, it can be concluded that the mode expansion approach developed in this study is a valuable tool that is capable of analyzing and designing MMFs for MMI-based applications. Considering that the mode expansion approach essentially uses a complete set of guided modes of a MMF, the field incident on the fiber can have complex polarization and amplitude distribution.

5. CONCLUSION

In this paper, the mode expansion approach in vectorial form, using a complete set of guided modes of a circular multimode SIF, is developed and employed to study the MMI of optical fields in MMFs for the first time, to the best of our knowledge. The properties of the characteristic equations that govern the propagation constants of guided modes are investigated, and a set of simplified formulas for the EM fields of modes with given propagation constants is introduced to systematically calculate the guided modes of a SIF with numerical procedures. Guided modes with negative angular orders, which are largely missing in literature, are adequately explored to develop a complete set of guided modes of a SIF necessary for the mode expansion approach. To facilitate the calculation of the mode expansion coefficients, a proper orthogonality relation between the guided modes of SIFs is identified and further validated numerically.

Based on the modal properties of an SIF and the orthogonality relation between guided modes, an adaptive algorithm designed for highly MMFs is derived to systematically and efficiently perform the mode expansion of optical fields in MMFs. The mode expansion approach is further employed to analyze the two MMI-based components—the coreless fiber segment in a monolithic MCF laser and the MMF segment in an SMF-MMF-SMF structure. For the cases that can be treated by FE-BPM and the diffraction theory, an excellent agreement is observed among the results from the mode expansion approach, the FE-BPM, and the diffraction theory. In addition, the mode-selection properties of the coreless fibers in MCF lasers, predicted by the mode expansion approach, are in good agreement with experimental observations. With the complete set of guided modes effectively utilized, incident fields are allowed to have complex polarization and amplitude distributions. As a result, the mode expansion approach developed in this study can resolve the polarization effect on MMI that cannot be captured by scalar approaches, providing a valuable tool for analyzing and designing MMFs for MMI-based applications.

Compared with other mode expansion approaches where circularly symmetric scalar modes are used and expansion coefficients are determined by evaluating one-dimensional integrations, the mode expansion approach presented here, although a vectorial one, also involves only one-dimensional integration with no significant increase in complexity and computational cost. It is worth noting that the concept of the adaptive mode expansion algorithm presented in this paper can be applied to other systems such as circularly symmetric gradient-index fibers.

APPENDIX A

In this section, the properties of the right sides of Eqs. (2a) and (2b) are discussed for EH and HE modes with angular order l greater than 1. To facilitate the derivation of the properties, Eqs. (2d) and (2e) are geometrically illustrated in Fig. 9, where the line segment n_2k_0 is perpendicular to the plane formed by line segments h and q.

The right side of Eq. (2a) can be expressed as

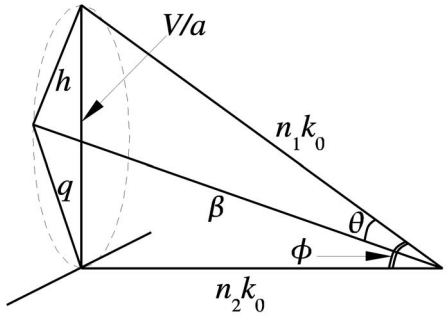

Fig. 9. Graphical representation of Eqs. (2d) and (2e).

$$\mathrm{RHS}_{\mathrm{EH}}(ha) = -RA + RB - R, \tag{A1a}$$

$$RA = -\frac{n_1^2+n_2^2}{2n_1^2}\frac{K_l'(qa)}{qaK_l(qa)} = \frac{n_1^2+n_2^2}{2n_1^2}\left(\frac{l}{(qa)^2}+\frac{K_{l-1}(qa)}{qaK_l(qa)}\right) > 0, \tag{A1b}$$

$$RB = l/(ha)^2. \tag{A1c}$$

When ha holds a value within the range of $(0,V)$, $\mathrm{RHS}_{\mathrm{EH}}$ is less than 0, since

$$\begin{aligned}\mathrm{RHS}_{\mathrm{EH}}(ha) &= -RA + RB - R < RB - R \\ &< \frac{l}{(ha)^2} - \frac{l\beta}{n_1k_0}\left(\frac{1}{(qa)^2}+\frac{1}{(ha)^2}\right) \\ &= -\left(1-\frac{\sin^2\phi}{1+\cos\theta}\right)\frac{l}{q^2a^2} < 0.\end{aligned} \tag{A2a}$$

When ha approaches the boundaries of range $(0,V)$, $\mathrm{RHS}_{\mathrm{EH}}$ takes an asymptotic form as follows:

$$\begin{aligned}\lim_{ha\to 0}\mathrm{RHS}_{\mathrm{EH}}(ha) &= \lim_{ha\to 0}\frac{(-RA+RB-R)(-RA+RB+R)}{(-RA+RB+R)} \\ &= -\frac{n_1^2+n_2^2}{2n_1^2}\left(\frac{2l}{V^2}+\frac{K_{l-1}(V)}{VK_l(V)}\right),\end{aligned} \tag{A2b}$$

$$\lim_{ha\to V}\mathrm{RHS}_{\mathrm{EH}}(ha) < \lim_{ha\to V}(-RA) = \lim_{qa\to 0}(-RA) \to -\infty. \tag{A2c}$$

Similarly, the right side of Eq. (2b) can be expressed as

$$\mathrm{RHS}_{\mathrm{HE}}(ha) = RA + RB - R. \tag{A3}$$

When ha holds a value within in the range of $(0,V)$, $\mathrm{RHS}_{\mathrm{HE}}$ is less than 0, since

$$\mathrm{RHS}_{\mathrm{HE}}(ha) = RA + RB - R = \mathrm{I}/(RA+RB+R), \tag{A4a}$$

$$\mathrm{I} = (RA+RB-R)(RA+RB+R) = \mathrm{I}_1 + \mathrm{I}_2, \tag{A4b}$$

$$\begin{aligned}\mathrm{I}_1 &= \frac{l^2}{(ha)^4} - \left(\frac{l\beta}{n_1k_0}\right)^2\left(\frac{1}{q^2a^2}+\frac{1}{h^2a^2}\right) \\ &\quad + \left(1+\frac{n_2^2}{n_1^2}\right)\frac{l^2}{(ha)^2(qa)^2} + \frac{n_2^2}{n_1^2}\frac{l^2}{(qa)^4} \\ &= \frac{l^2}{(qa)^4}\left[-\left(\frac{2\sin^2\phi}{\sin^2\theta}-1-\frac{\sin^4\phi}{\sin^2\theta}\right)\right. \\ &\quad \left. + \left(\frac{\sin^2\phi}{\sin^2\theta}-1\right)(2-\sin^2\phi) + (1-\sin^2\phi)\right] = 0,\end{aligned}$$

$$\mathrm{I}_2 = \frac{K_{l-1}(qa)}{qaK_l(qa)}\left[\frac{l}{(ha)^2}+\frac{n_2^2}{n_1^2}\left(\frac{l}{(ha)^2}+\frac{2l}{(qa)^2}+\frac{K_{l-1}(qa)}{qaK_l(qa)}\right)\right] > 0. \tag{A4c}$$

When ha approaches the boundaries of range $(0,V)$, $\mathrm{RHS}_{\mathrm{HE}}$ takes an asymptotic form as follows:

$$\lim_{ha\to 0}\mathrm{RHS}_{\mathrm{HE}}(ha) = \lim_{ha\to 0}\frac{\mathrm{I}}{(RA+RB+R)} = \frac{n_1^2+n_2^2}{2n_1^2}\frac{K_{l-1}(V)}{VK_l(V)}, \tag{A5a}$$

$$\begin{aligned}\lim_{ha\to V}\mathrm{RHS}_{\mathrm{HE}}(ha) &= \lim_{qa\to 0}\frac{\mathrm{I}}{(RA+RB+R)} \\ &= \lim_{qa\to 0} -\frac{2n_2^2}{n_1^2+n_2^2}\ln(qa) \\ &\to +\infty \quad \text{for } l=1,\end{aligned} \tag{A5b}$$

$$\lim_{ha\to V}\mathrm{RHS}_{\mathrm{HE}}(ha) = \frac{1}{l-1}\frac{n_2^2}{n_1^2+n_2^2} \quad \text{for } l>1. \tag{A5c}$$

Note that two limiting properties of $K_l(x)$ [15,33,34],

$$K_0(x)/(xK_1(x)) \to -\ln x, \tag{A6a}$$

$$K_{l-1}(x)/(xK_l(x)) \to -1/(2(l-1)) \tag{A6b}$$

for x approaching 0, are employed in these derivations.

APPENDIX B

The orthogonality properties of the guided modes of a generalized bidirectional SIF, as illustrated in Fig. 10, are

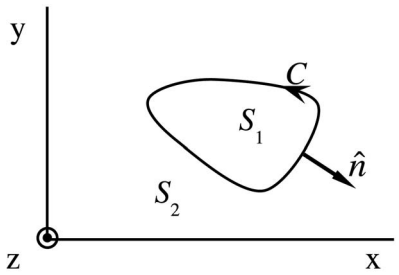

Fig. 10. Schematic of the cross section of a generalized SIF.

discussed in this section. In Fig. 10, S_1 and S_2 correspond to the core and cladding regions of the step-index fiber, respectively; C is the interface between S_1 and S_2, going counterclockwise; and $\hat{n}$ is the unit outward normal. Let $(\vec{E}^{(n)}, \vec{H}^{(n)})$ and $(\vec{E}^{(m)}, \vec{H}^{(m)})$ be two linearly independent solutions to Maxwell's equations for monochromatic fields of frequency ω; the Lorentz reciprocal principle can be expressed in a differential form as follows [21]:

$$\nabla \cdot (\vec{E}^{(n)} \times \vec{H}^{(m)} - \vec{E}^{(m)} \times \vec{H}^{(n)}) = 0, \tag{B1}$$

where no free or bond charge is present in the system. If $\vec{E}^{(n)}$ and $\vec{H}^{(n)}$ are the EM fields of the normal mode n of the fiber in Fig. 10, they can be written as [16,19,21,22]:

$$\vec{E}^{(n)} = \vec{E}_T^{(n)} + \vec{E}_z^{(n)}\hat{z} = (\vec{e}_T^{(n)}(x,y) + e_z^{(n)}(x,y)\hat{z})\exp(-\Gamma_n z), \tag{B2a}$$

$$\vec{H}^{(n)} = \vec{H}_T^{(n)} + \vec{H}_z^{(n)}\hat{z} = (\vec{h}_T^{(n)}(x,y) + h_z^{(n)}(x,y))\exp(-\Gamma_n z), \tag{B2b}$$

where the subscript T denotes the transverse component and Γ_n is a complex number (or a purely imaginary number for a lossless fiber). Note that the modes considered here are confined in the x–y plane. For normal modes m and n, Eq. (B1) reduces to

$$\nabla_T \cdot (\vec{E}^{(n)} \times \vec{H}^{(m)} - \vec{E}^{(m)} \times \vec{H}^{(n)}) = (\Gamma_n + \Gamma_m)\hat{z} \cdot (\vec{E}^{(n)} \times \vec{H}^{(m)} - \vec{E}^{(m)} \times \vec{H}^{(n)}). \tag{B3}$$

With the two-dimensional form of the divergence theorem, Eq. (B3) can be written in an integral form as

$$(\Gamma_n + \Gamma_m)\iint_{S_1+S_2} dS(\vec{E}^{(n)} \times \vec{H}^{(m)} - \vec{E}^{(m)} \times \vec{H}^{(n)}) \cdot \hat{z} = \oint_C dl[(\vec{E}^{(n)}\vec{H}^{(m)} - \vec{E}^{(m)} \times \vec{H}^{(n)})^{(1)} - (\vec{E}^{(n)} \times \vec{H}^{(m)} - \vec{E}^{(m)} \times \vec{H}^{(n)})^{(2)}] \cdot \hat{n}, \tag{B4}$$

where the superscripts (1) and (2) represent the fields in the regions of S_1 and S_2, respectively. With the relation of

$$(\vec{E}^{(n)} \times \vec{H}^{(m)}) \cdot \hat{n} = (\vec{E}_T^{(n)} \times H_z^{(m)}\hat{z} + E_z^{(n)}\hat{z} \times \vec{H}_T^{(m)}) \cdot \hat{n}, \tag{B5}$$

and the continuity of the tangential components of the fields along the interface C, the right side of Eq. (B4) reduces to

$$RS = \oint_C dl[(\vec{E}_T^{(n)(1)} - \vec{E}_T^{(n)(2)})H_z^{(m)} - (\vec{E}_T^{(m)(1)} - \vec{E}_T^{(m)(2)})H_z^{(n)}] \times \hat{z} \cdot \hat{n}. \tag{B6}$$

Given that

$$\vec{E}_T^{(n)(1)} - \vec{E}_T^{(n)(2)} = (E_{TN}^{(n)(1)} - E_{TN}^{(n)(2)})\hat{n}, \tag{B7}$$

where N in the subscript denotes the component of the transverse field in the direction of $\hat{n}$, Eq. (B6) reduces to

$$RS = \oint_C dl[(E_{TN}^{(n)(1)} - E_{TN}^{(n)(2)})\hat{n}H_z^{(m)} - (E_{TN}^{(m)(1)} - E_{TN}^{(m)(2)})\hat{n}H_z^{(n)}] \times \hat{z}\hat{n} = 0. \tag{B8}$$

The combination of Eqs. (B2a), (B2b), (B4), (B6), and (B8) leads to the final result of

$$(\Gamma_n + \Gamma_m)\iint_{S_1+S_2} dS(\vec{e}_T^{(n)} \times \vec{h}_T^{(m)} - \vec{e}_T^{(m)} \times \vec{h}_T^{(n)}) \cdot \hat{z} = 0. \tag{B9}$$

Then, Eq. (14) is obtained for bidirectional waveguides (fibers) by following the same procedure in [21], with the integration region S replaced by regions S_1 and S_2.

For lossless fibers, the Lorentz reciprocal principle can be written as

$$\nabla \cdot (\vec{E}^{(n)} \times \vec{H}^{(m)*} + \vec{E}^{(m)*} \times \vec{H}^{(n)}) = 0, \tag{B10}$$

and Eq. (15) can be similarly derived. Note that Eqs. (14) and (15) are both valid for lossless fibers since they are automatically bidirectional [22]. For a fiber with loss or gain, bidirectionality can be ensured by specific spatial symmetries of the fiber. Interested readers are referred to [22] for details on bidirectionality.

It needs to be pointed out that the derivation for Eqs. (14) and (15) is valid for modes m and n with $\Gamma_m \neq \Gamma_n$ (or nondegenerate modes). For a set of degenerate modes of a lossless fiber, an independent set of modes can be formed by linear superposition of the modes in the original set so that Eqs. (14) and (15) can be selectively satisfied by the modes in the new set [23].

ACKNOWLEDGMENTS

This work is supported by the Air Force Office of Scientific Research through an MRI program F49620-02-1-0380. The authors would like to thank A. Mafi of Corning Inc. for his inspiring input and S. Honkanen of Helsinki University of Technology for reviewing part of the work.

REFERENCES

1. A. Mehta, W. S. Mohammed, and E. G. Johnson, "Multimode interference-based fiber-optic displacement sensor," IEEE Photon. Technol. Lett. **15**, 1129–1131 (2003).
2. W. S. Mohammed, A. Mehta, and E. G. Johnson, "Wavelength tunable fiber lens based on multimode interference," J. Lightwave Technol. **22**, 469–477 (2004).
3. R. Selvas, I. Torres-Gomez, A. Martinez-Rios, J. Alvarez-Chavez, D. May-Arrioja, P. LiKamWa, A. Mehta, and E. Johnson, "Wavelength tuning of fiber lasers using multimode interference effects," Opt. Express **13**, 9439–9445 (2005).
4. Q. Wang and G. Farrell, "All-fiber multimode-interference-based refractometer sensor: proposal and design," Opt. Lett. **31**, 317–319 (2006).
5. W. S. Mohammed, P. W. E. Smith, and X. Gu, "All-fiber multimode interference bandpass filter," Opt. Lett. **31**, 2547–2549 (2006).
6. L. Li, A. Schülzgen, S. Chen, V. L. Temyanko, J. V. Moloney, and N. Peyghambarian, "Phase locking and in-phase supermode selection in monolithic multicore fiber lasers," Opt. Lett. **31**, 2577–2579 (2006).
7. L. Li, A. Schülzgen, H. Li, V. L. Temyanko, J. V. Moloney, and N. Peyghambarian, "Phase-locked multicore all-fiber

lasers: modeling and experimental investigation," J. Opt. Soc. Am. B **24**, 1721–1728 (2007).
8. O. Bryngdahl, "Image formation using self-imaging techniques," J. Opt. Soc. Am. **63**, 416–419 (1973).
9. R. Ulrich, "Image formation by phase coincidences in optical waveguides," Opt. Commun. **13**, 259–264 (1975).
10. L. B. Soldano and E. C. M. Pennings, "Optical multi-mode interference devices based on self-imaging: principles and applications," J. Lightwave Technol. **13**, 615–627 (1995).
11. Q. Wang and G. Farrell, "Numerical investigation of multimode interference in a multimode fiber and its applications in optical sensing," Proc. SPIE **6189**, 61891N (2006).
12. E. Snitzer, "Cylindrical dielectric waveguide modes," J. Opt. Soc. Am. **51**, 491–498 (1961).
13. N. S. Kapany and J. J. Burke, *Optical Waveguides* (Academic, 1972).
14. A. W. Snyder and J. D. Love, *Optical Waveguide Theory* (Chapman and Hall, 1983).
15. A. Yariv, *Optical Electronics in Modern Communications* (Oxford U. Press, 1997).
16. R. B. Adler, "Properties of guided waves on inhomogeneous cylindrical structures," Research Laboratory of Electronics, Massachusetts Institute of Technology, Tech. Rep. 102 (1949).
17. L. R. Walker, "Orthogonality relation for gyrotropic waveguides," J. Appl. Phys. **28**, 377 (1957).
18. A. D. Bresler, G. H. Joshi, and N. Marcuvitz, "Orthogonality properties of modes in passive and active uniform wave guides," J. Appl. Phys. **29**, 794–799 (1958).
19. A. T. Villeneuve, "Orthogonality relationships for waveguides and cavities with inhomogeneous anisotropic media," IRE Trans. Electron Devices **MTT-7**, 441–446 (1959).
20. L. B. Felsen and N. Marcuvitz, *Radiation and Scattering of Waves* (Prentice-Hall, 1973).
21. R. E. Collin, *Field Theory of Guided Waves* (IEEE, 1991).
22. P. R. McIsaac, "Mode orthogonality in reciprocal and nonreciprocal waveguides," IEEE Trans. Microwave Theory Tech. **39**, 1808–1816 (1991).
23. C. Vassallo, *Optical Waveguide Concepts* (Elsevier, 1991).
24. A. Hardy and M. Ben-Artzi, "Expansion of an arbitrary field in terms of waveguide modes," IEE Proc.: Optoelectron. **141**, 16–20 (1994).
25. K. M. Gundu, M. Brio, and J. V. Moloney, "A mixed high-order vector finite element method for waveguides: convergence and spurious mode studies," Int. J. Numer. Model. **18**, 351–364 (2005).
26. K. M. Gundu, College of Optical Sciences, the University of Arizona, 1630 East University Boulevard, Tucson, Arizona 85721, USA (personal communication, 2006).
27. G. R. Hadley, "Wide-angle beam propagation using Padé approximant operators," Opt. Lett. **17**, 1426–1428 (1992).
28. M. Wrage, P. Glas, D. Fisher, M. Leitner, D. D. Vysotsky, and A. P. Napartovich, "Phase locking in a multicore fiber laser by means of a Talbot resonator," Opt. Lett. **25**, 1436–1438 (2000).
29. A. Mafi and J. V. Moloney, "Phase locking in a passive multicore photonic crystal fiber," J. Opt. Soc. Am. B **21**, 897–902 (2004).
30. L. Michaille, C. R. Bennett, D. M. Taylor, T. J. Shepherd, J. Broeng, H. R. Simonsen, and A. Petersson, "Phase locking and supermode selection in multicore photonic crystal fiber lasers with a large doped area," Opt. Lett. **30**, 1668–1670 (2005).
31. http://www.ece.byu.edu/photonics/connectors.parts/smf28.pdf.
32. P.-L. Liu and S. De, "Fiber design—from optical mode to index profile," Opt. Eng. (Bellingham) **42**, 981–984 (2003).
33. G. Arfken, *Mathematical Methods for Physicists* (Academic, 1985).
34. M. Abramowitz and I. A. Stegun, eds., *Handbook of Mathematical Functions with Formulas, Graphs, and Mathematical Tables* (U.S. Govternment Printing Office, 1972).